ARTICLES
https://doi.org/10.1038/s41563-022-01329-8

nature materials

Check for updates

Nuclear spin polarization and control in hexagonal boron nitride

Xingyu Gao[1], Sumukh Vaidya[1], Kejun Li[2], Peng Ju[1], Boyang Jiang[3], Zhujing Xu[1], Andres E. Llacsahuanga Allcca[1], Kunhong Shen[1], Takashi Taniguchi[4], Kenji Watanabe[5], Sunil A. Bhave[3,6,7], Yong P. Chen[1,3,6,7,8], Yuan Ping[9] and Tongcang Li[1,3,6,7] ✉

Electron spins in van der Waals materials are playing a crucial role in recent advances in condensed-matter physics and spintronics. However, nuclear spins in van der Waals materials remain an unexplored quantum resource. Here we report optical polarization and coherent control of nuclear spins in a van der Waals material at room temperature. We use negatively charged boron vacancy (V_B^-) spin defects in hexagonal boron nitride to polarize nearby nitrogen nuclear spins. We observe the Rabi frequency of nuclear spins at the excited-state level anti-crossing of V_B^- defects to be 350 times larger than that of an isolated nucleus, and demonstrate fast coherent control of nuclear spins. Further, we detect strong electron-mediated nuclear–nuclear spin coupling that is five orders of magnitude larger than the direct nuclear-spin dipolar coupling, enabling multi-qubit operations. Our work opens new avenues for the manipulation of nuclear spins in van der Waals materials for quantum information science and technology.

Since the discovery of graphene, van der Waals (vdW) layered materials have been a focus of materials research for the last two decades[1–5]. Owing to their weak interlayer interaction, vdW materials can be readily exfoliated and integrated with different materials and structures[4,5]. Electron spins in vdW materials played essential roles in recent development in spintronics and condensed-matter physics, including topological insulators[6–8], two-dimensional (2D) magnets[9,10] and spin liquids[11,12]. Most vdW materials also have non-zero nuclear spins, which have applications in quantum sensing and quantum information processing if they can be efficiently polarized and coherently controlled[13–15]. Nuclear spins in liquids have been used to perform quantum algorithms with conventional nuclear magnetic resonance (NMR) systems[16]. However, the thermal polarization of nuclear spins is extremely low in realistic magnetic fields at room temperature because of their small gyromagnetic ratio[16]. Recently, it was theoretically proposed to couple a 2D lattice of nuclear spins to a diamond nitrogen-vacancy centre for large-scale quantum simulation[15]. However, the achieved coupling has been too weak to use a diamond nitrogen-vacancy centre to polarize nuclear spins in a vdW material so far[17]. To the best of our knowledge, there is still no report on the efficient polarization and coherent control of nuclear spins in a vdW material.

Here we report the experimental demonstration of optical polarization and coherent control of nuclear spins in a vdW material. We utilize the recently discovered boron vacancy (V_B^-) spin defects in hexagonal boron nitride (hBN)[18–22] to polarize the three nearest ^{14}N nuclear spins around each V_B^- electron spin (Fig. 1). Note that hBN has a crystalline structure similar to that of graphene but has a large bandgap typically in the range of 5–6 eV, making it an ideal vdW material host for optically addressable spin defects[18,23–25]. So far, the most studied spin defect in hBN is the V_B^- defect[20–22], which can be generated by ion implantation[26–28] and other methods[18,29]. Note that V_B^- spin defects have a high optically detected magnetic resonance (ODMR) contrast[27], and have been used for the quantum sensing[27,30] and quantum imaging of 2D magnetic materials[31,32]. Different from diamond that has sparse nuclear spins[33], all the atoms in hBN have non-zero nuclear spins. Because they have longer coherence times than those of electron spins, nuclear spins are promising resources for quantum sensing, network, computing and simulation if they can be polarized and coherently controlled[15,33–35].

In this Article, we optically polarize nuclear spins in hBN at room temperature using the hyperfine interaction (HFI) between nuclear spins and V_B^- electron spins (Fig. 1). Our hBN sample is ion implanted using 2.5 keV helium ions with a dose density of 10^{14} cm^{-2}. Roughly 10^5 V_B^- defects are polarized by a tightly focused 532 nm laser. We only consider ^{14}N nuclei in this work since 99.6% of natural nitrogen is ^{14}N, which has spin 1. We use plasmonic enhancement to speed up optical polarization and readout of V_B^- spin defects (Supplementary Fig. 1)[27]. The achieved average polarization of the three nearest ^{14}N nuclear spins around each V_B^- spin defect is about 32% near the excited-state level anti-crossing (ESLAC) and is even larger near the ground-state level anti-crossing (GSLAC). Thus, these nuclear spins are cooled to less than 1 mK with optical pumping when the environment is at room temperature. With polarized nuclear spins in hBN, we implement the optically detected nuclear magnetic resonance (ODNMR). The measured ODNMR spectra of the three trigonal nearest nitrogen nuclear spins show strong nuclear–nuclear coupling mediated by electron spins[36], which is 10^5 times larger than the direct nuclear-spin dipolar coupling. We also perform ab initio calculations[37–39] to support our observations. Last, we resonantly drive the nuclear spin transition and realize coherent control of nitrogen nuclear spin states. Remarkably, the

[1]Department of Physics and Astronomy, Purdue University, West Lafayette, IN, USA. [2]Department of Physics, University of California, Santa Cruz, CA, USA. [3]Elmore Family School of Electrical and Computer Engineering, Purdue University, West Lafayette, IN, USA. [4]International Center for Materials Nanoarchitectonics, National Institute for Materials Science, Tsukuba, Japan. [5]Research Center for Functional Materials, National Institute for Materials Science, Tsukuba, Japan. [6]Purdue Quantum Science and Engineering Institute, Purdue University, West Lafayette, IN, USA. [7]Birck Nanotechnology Center, Purdue University, West Lafayette, IN, USA. [8]WPI-AIMR International Research Center for Materials Sciences, Tohoku University, Sendai, Japan. [9]Department of Chemistry and Biochemistry, University of California, Santa Cruz, CA, USA. ✉e-mail: tcli@purdue.edu

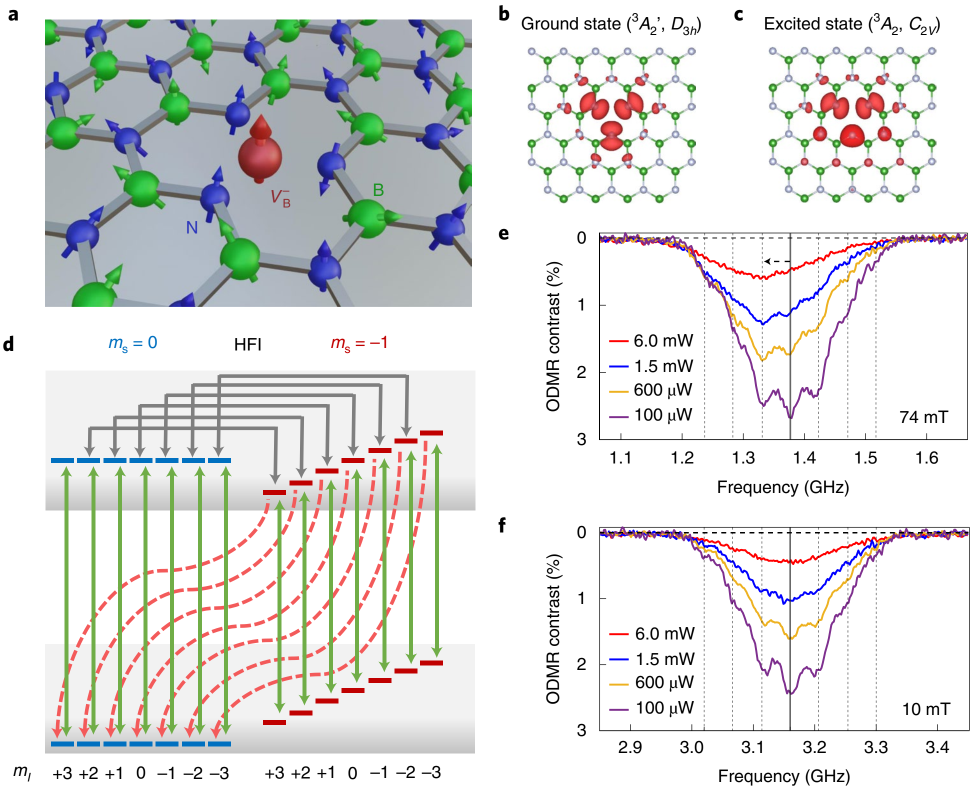

Fig. 1 | Optical polarization of nuclear spins in hBN with V_B^- spin defects. **a**, Illustration of nuclear spins around a V_B^- defect in a 2D hBN lattice. Both nitrogen (blue) and boron (green) atoms have non-zero nuclear spins. The electron spin of the V_B^- defect (red sphere) couples to the three nearest nitrogen nuclear spins via HFI. **b**, GS electron spin density of a V_B^- defect. **c**, ES spin density of a V_B^- defect. **d**, Simplified diagram illustrating the dynamics of optical spin polarization at ESLAC. The red dashed lines indicate non-radiative transitions and the green solid lines represent optical transitions that conserve nuclear spins. The grey arrows show the transverse HFI that hybridize the electron–nuclear spin states. **e**,**f**, ODMR spectra of V_B^- defects at ESLAC (**e**) and in a weak magnetic field far from ESLAC (**f**). The dashed lines are guides for eyes, showing the expected positions of hyperfine peaks. The horizontal dashed arrow shows the centre shift under laser excitation with different powers. The microwave power is $P_{MW} = 5$ mW.

Rabi oscillation of nuclear spins is enhanced by a factor of about 350 near ESLAC due to HFI. Utilizing hyperfine enhancement, we achieve megahertz-level fast coherent control of nuclear spins.

Optical polarization of nuclear spins in hBN. As shown in Fig. 1a, a V_B^- spin defect is formed by missing a boron atom in the hBN lattice. The V_B^- defect has a spin-triplet ground state (GS) with zero-field splitting (ZFS) of $D_{GS} = 3.45$ GHz (ref. [18]), and a spin-triplet excited state (ES) with ZFS of $D_{ES} = 2.1$ GHz (refs. [40–43]). The spin-dependent state recombination and photon emission allow optical initialization and readout of the electron spin state (Supplementary Fig. 2). The V_B^- electron spin couples to nuclear spins via HFI. As the HFI with farther nuclear spins is much weaker[21], we only consider the three nearest ^{14}N nuclear spins in this work. The spin system of V_B^- defects can be described by the same form of the Hamiltonian for both GS (Fig. 1b) and ES (Fig. 1c and Supplementary Figs. 3 and 4) using different parameters. The GS (as well as ES) Hamiltonian in the presence of an external magnetic field B_0 includes electron spin–spin interaction (ZFS), electron–nuclear HFI, electron and nuclear Zeeman splitting, and nuclear-spin quadrupole interaction:

$$H = D[S_z^2 - S(S+1)/3] + \sum_{j=1,2,3} \mathbf{S}\mathbf{A}_j\mathbf{I}_j + \gamma_e B_0 S_z - \sum_{j=1,2,3} \gamma_n B_0 I_{zj} + \sum_{j=1,2,3} Q_j(I_{zj}^2 - I_j(I_j+1)/3). \quad (1)$$

Here D is the ZFS parameter, $\mathbf{S}$ and S_z are the electron spin-1 operators, $\mathbf{I}_j$ and I_{zj} ($j = 1,2,3$) are the nuclear spin-1 operators of the three nearest ^{14}N nuclei, $\mathbf{A}_j$ is the HFI tensor, $\gamma_e = 28$ GHz T^{-1} is the electron-spin gyromagnetic ratio, $\gamma_n = 3.076$ MHz T^{-1} is the gyromagnetic ratio of ^{14}N nuclear spin and Q_j is the quadrupole coupling constant. The z axis is perpendicular to the hBN nanosheet.

As shown in Fig. 1d, in a magnetic field corresponding to the level anti-crossing (about 74 mT for ES and 124 mT for GS), the sublevels with electron spin $m_s = -1$ approach the sublevels with electron spin $m_s = 0$. The transverse HFI then hybridizes the state $|m_s = 0, m_I\rangle$ and state $|m_s = -1, m_I + 1\rangle$ (here we denote m_I as the total z component of the three nearest ^{14}N nuclei). Continuous optical pumping keeps initializing the electron spin state into the $m_s = 0$ state as nuclear spin m_I is conserved. Meanwhile, by means of state mixing, the total spin state has a chance to evolve into $|m_s = -1, m_I + 1\rangle$ in each optical cycle[44]. In the ideal case, the spin system is eventually polarized into an un-mixed $|m_s = 0, m_I = 3\rangle$ state.

In the experiment, we use a 532 nm laser to polarize nuclear spins at room temperature and use ODMR to measure the nuclear spin distribution. First, we use a low-power laser (100 μW) for spin initialization and readout (Figs. 1e and 2a), which avoids power broadening and has a mild effect on nuclear spin polarization. As a result, the hyperfine structure is clearly resolved and the ODMR spectrum is almost symmetric around the centre peak ($m_I = 0$), indicating low nuclear spin polarization. When we increase the laser power, substantial distortion and shift of the ODMR spectrum are observed at 74 mT (Figs. 1e and 2b), indicating large polarization of nuclear spins. In contrast, in a 10 mT magnetic field, the centre nearly remains at the same position under different laser-power excitation levels (Fig. 1f).

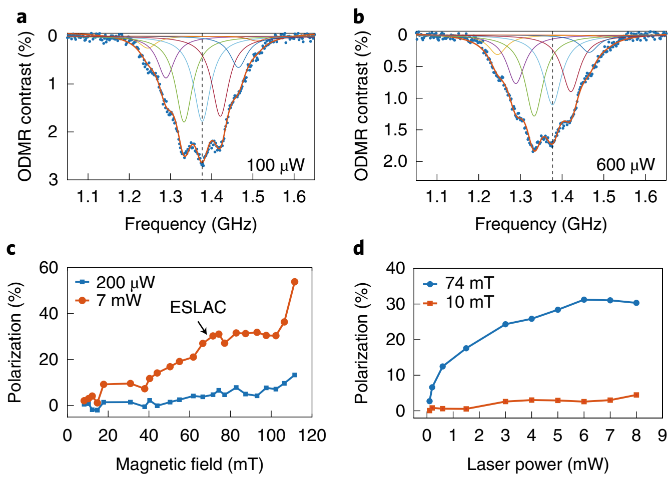

Fig. 2 | Polarization of the three nearest nitrogen nuclear spins. a,**b**, ODMR spectrum at ESLAC under laser excitation of 100 μW (**a**) and 600 μW (**b**). The experimental data are fit using seven Lorentzian curves corresponding to $m_I = +3, +2, +1, 0, -1, -2, -3$. The frequency of each hyperfine peak is obtained from the fitting results using the data of 100 μW, and does not change for higher laser powers. The centre dashed vertical line marks the hyperfine peak at $m_I = 0$. **c**, Measured average polarization of the three nearest nitrogen nuclear spins as a function of the magnetic field. The nuclear spin polarization increases when the magnetic field increases from 7 to 110 mT. A strong laser excitation (7 mW, red curve) produces a larger polarization than that with a weak laser excitation (200 μW, blue curve). **d**, Nuclear spin polarization as a function of excitation laser power at ESLAC (74 mT, blue curve) and in a small magnetic field (10 mT, red curve). The microwave power is $P_{MW} = 5$ mW.

The average polarization of the three nearest ^{14}N nuclear spins is measured as $P_{\rm exp} = \sum_{m_I} m_I \rho_{m_I} / (3 \sum_{m_I} \rho_{m_I})$, where the summation is performed over the seven hyperfine peaks in the ODMR spectrum. Here ρ_{m_I} denotes the fitted relative population of the m_I states (Fig. 2 and Methods). Figure 2c shows the nuclear spin polarization $P_{\rm exp}$ as a function of magnetic fields. In a weak magnetic field that is far from ESLAC, $P_{\rm exp}$ is small. Around ESLAC, $P_{\rm exp}$ increases when the laser power increases, and reaches 32% under high-laser-power excitation (6 mW) (Fig. 2d). This polarization would require a magnetic field of about 10^6 T if they were polarized by thermal distribution at room temperature. The nuclear spin polarization increases further and exceeds 50% near the GSLAC. Supplementary Figs. 5 and 6 provide numerical simulation data of the optical polarization process.

Optically detected NMR. With polarized nuclear spins, we conduct ODNMR experiments to gain more insights into the coupled electron–nuclear spin system in hBN (Fig. 3). We first implement the electron–nuclear double resonance (ENDOR) technique to obtain the ODNMR spectroscopy of the three nearest ^{14}N nuclei (Fig. 3d). After initializing the system into the $|m_s = 0, m_I\rangle$ state using a 7 mW laser pulse, a selective microwave (MW) π pulse is applied on the electron spin to transfer the population to the $|m_s = -1, m_I\rangle$ state. Then, we use a radio-frequency (RF) pulse to drive nuclear spin transitions to change the nuclear spin state from m_I to m'. Finally, optical readout is performed after applying another MW π pulse that transfers the population back from $|m_s = -1, m'\rangle$ to $|m_s = 0, m'\rangle$. The ODNMR spectrum is presented in Fig. 3e. We observe a broad peak at around 45 MHz due to nuclear spin transitions among the $|m_s = -1, m_I\rangle$ states. The centre of the peak is close to the HFI constant $A_{zz} = 47$ MHz. Meanwhile, there is another broad peak at around 5 MHz due to nuclear spin transitions among the $|m_s = 0, m_I\rangle$ states. To confirm our observation, we perform another ODNMR measurement without the MW pulse as the 'reference' (Fig. 3d,e). Under this condition, the electron spin stays in the $m_s = 0$ state after laser initialization. Therefore, there is no HFI. As a result, the signal at around 45 MHz in the reference ODNMR spectrum is negligible. Meanwhile, the magnitude of the peak at around 5 MHz increases because more electron spins stay in the $m_s = 0$ state. These results confirm that the electron spins of V_B^- defects are polarized to the $m_s = 0$ state instead of the $m_s = \pm 1$ states after laser initialization.

We support our experimental findings by modelling the system using the full Hamiltonian (equation (1)) that consists of a V_B^- electron spin and the three nearest ^{14}N nuclear spins. Due to HFI between the three ^{14}N nuclear spins and electron spin, there are 27 energy sublevels for the $m_s = -1$ branch (Fig. 3c). As presented in Fig. 3f, these sublevels result in many allowed nuclear spin transitions over a broad frequency range. This causes broadening in our measured ODNMR spectrum (Fig. 3g). Our simulated NMR spectrum agrees well with the experimental results (Fig. 3h and Supplementary Figs. 7 and 9). With a weaker but longer RF pulse, we can resolve a narrow peak near 52 MHz (Fig. 3i).

The broad distribution of allowed transitions in ODNMR is due to the strong nuclear–nuclear coupling mediated by the electron spin[36]. These three ^{14}N nuclear spins are strongly coupled to the same electron spin via HFI. When the system is far away from the GSLAC ($|D_{\rm GS} - \gamma_e B| \gg A_{xx}, A_{yy}, A_{zz}$), the effective nuclear–nuclear spin coupling constant is $C_{\rm NN} = A_{\rm tran}^2 / |D_{\rm GS} - \gamma_e B|$ for the $m_s = -1$ branch, where $A_{\rm tran} = (A_{xx} + A_{yy})/2 = 68$ MHz is the transverse HFI constant (Supplementary Table 1). At 74 mT, $C_{\rm NN} = 3.4$ MHz, which is 10^5 times larger than the direct nuclear-spin dipolar coupling constant $d_{\rm NN} = \mu_0 (\gamma_n)^2 \hbar / (2 r_{\rm NN}^3) = 34$ Hz (Supplementary Fig. 12). Here μ_0 is the vacuum permeability, $\hbar = h/(2\pi)$ and $r_{\rm NN}$ is the separation between two nearest nitrogen nuclei. Further, $C_{\rm NN}$ is large near GSLAC, but decreases when the magnetic field is very large: $C_{\rm NN} = 50$ kHz at 3.3 T. Thus, the profiles of our measured ODNMR spectra at 74 mT are very different from the results obtained at 3.3 T using a commercial pulsed electron spin resonance spectrometer (Supplementary Fig. 9 provides a detailed numerical analysis)[45]. Because of the small $C_{\rm NN}$ in a large magnetic field, the former work with V_B^- spin defects at 3.3 T did not observe nuclear–nuclear spin interaction[45]. Our observation of strong megahertz-level nuclear–nuclear coupling will be important for multi-qubit quantum gates.

Coherent control of nuclear spins in hBN. We now perform the coherent control of nuclear spins in hBN. For an isolated ^{14}N nucleus, its Rabi frequency is $\gamma_e / \gamma_n = 9{,}110$ times smaller than that of an electron spin, making it challenging to perform coherent control. However, the V_B^- electron spin can increase the Rabi frequency of the nearby nuclear spins by hyperfine enhancement. Because of the large γ_e / γ_n ratio, even a slight coupling can lead to large enhancement in the Rabi frequency[46,47]. We use the $m_s = -1$ electron state because it gives larger hyperfine enhancement (Supplementary Fig. 11). We observe Rabi oscillations by performing ODNMR experiments using a 52 MHz RF drive with a varying pulse length. Figure 4a–c illustrates the Rabi oscillations of the nuclear spin state under different RF driving powers. By fitting the Rabi oscillation, we estimate the inhomogeneous coherence time T_{2n}^* of nuclear spins to be about 3.5 μs at room temperature. This T_{2n}^* is much longer than the inhomogeneous coherence time T_{2e}^* of V_B^- electron spins, which is about 96 ns (Supplementary Fig. 10). The Rabi frequency shows a good linear dependence on the square root of the RF power (Fig. 4d). By comparing the Rabi frequencies of electron spin and nuclear spin, we find that the Rabi frequency of the ^{14}N nuclear spin is enhanced by a factor of 350 at ESLAC, which enables fast coherent control. A simplified theoretical model predicts the hyperfine enhancement of nuclear spins coupled to the $m_s = -1$ electron state to be about 420

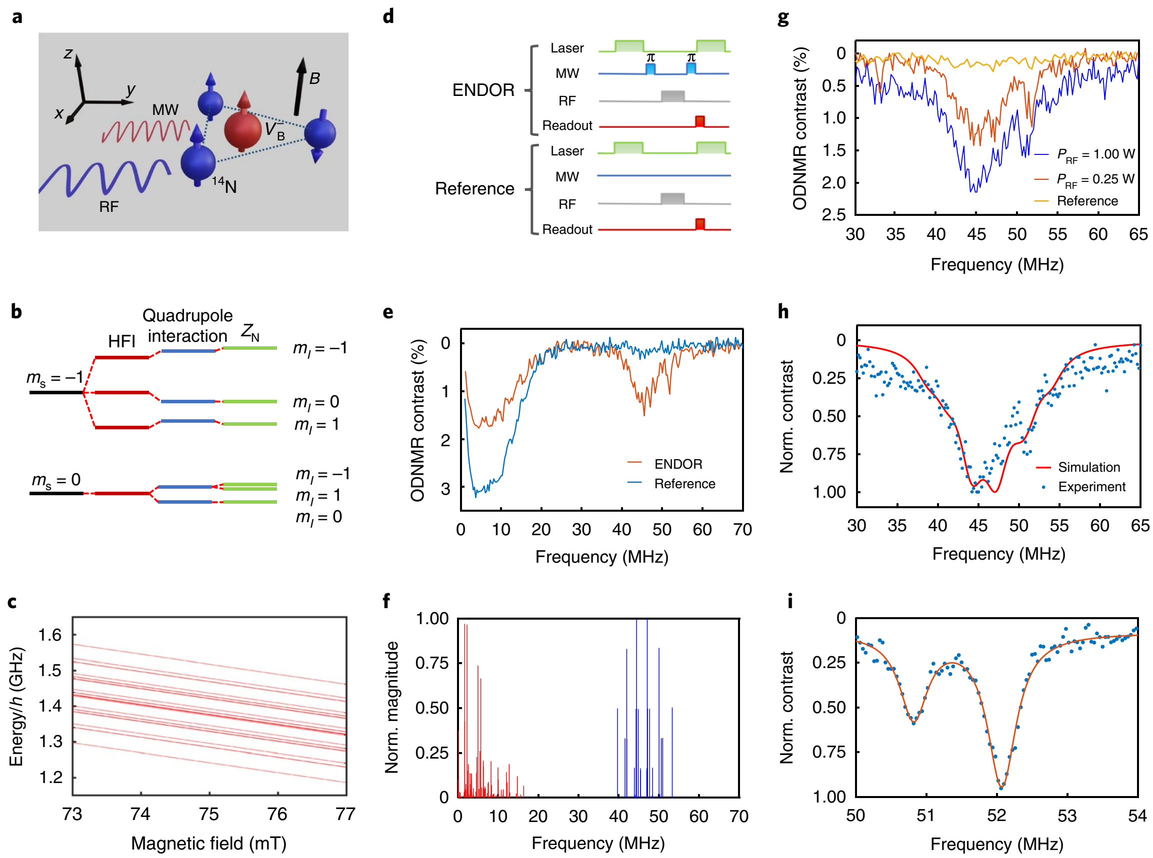

Fig. 3 | ODNMR spectroscopy of the three nearest nitrogen nuclear spins. a, Schematic of a V_B^- defect coupled to three nearest nitrogen nuclear spins. An external static magnetic field (B) is applied perpendicular to the hBN flake. An RF pulse generates an in-plane a.c. magnetic field that drives nuclear spin transitions. An MW pulse drives electron spin transitions. **b**, Energy-level diagram for an electron spin coupled to a nuclear spin in a magnetic field. The interactions include ZFS, electron-spin Zeeman effect, HFI, quadrupole interaction and nuclear-spin Zeeman effect (Z_N). **c**, Simulated electron-spin energy levels around ESLAC, which has 27 lines for the $m_s = -1$ branch; h denotes the Planck constant. **d**, Schematic of the ODNMR pulse sequences. **e**, Large-range scan of the ODNMR spectrum. Using the ENDOR sequence, a broad peak at around 45 MHz is observed (red curve), whereas this peak disappears when there are no MW π pulses (blue curve). **f**, Simulated nuclear spin transitions. **g**, More detailed measurement of the ODNMR spectrum for the $m_s = -1$ branch. **h**, Comparison between the experimental result and numerical simulation, which shows good agreement. **i**, Isolating a nuclear spin transition by using a weak RF drive (P_{RF} = 0.06 W) for a longer duration. The microwave power is P_{MW} = 0.35 W. The external magnetic field is 74 mT.

at ESLAC (Supplementary Fig. 11). Thus, the experimental result shows good agreement with the theoretical prediction.

In conclusion, we have optically polarized nuclear spins in a vdW material with intrinsic electron spin defects. By making use of ESLAC and GSLAC of V_B^- spin defects in hBN, we are able to polarize the three nearest ^{14}N nuclear spins at room temperature over a broad range of magnetic fields. Our ODNMR measurements show the NMR spectrum using the intrinsic spin defects of hBN. This further reveals the strong nuclear–nuclear spin coupling mediated by electron spin, which could enable multi-qubit operations. We also demonstrate megahertz-level coherent control of nuclear spins with hyperfine enhancement. The polarized nuclear spins in vdW materials have potential applications in quantum sensing, network, computing and simulation[13–15,33–35]. Nitrogen nuclear spins in the

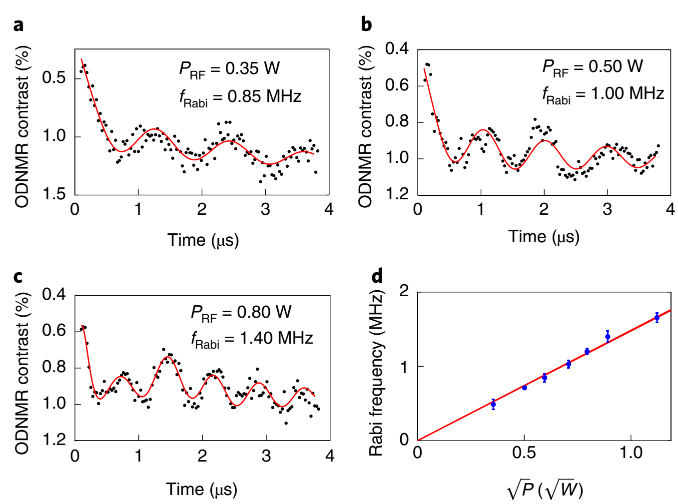

Fig. 4 | Coherent control of nuclear spins in hBN. a–c, ODNMR contrasts as functions of RF-pulse duration times τ when the driving RF power is 0.35 W (**a**), 0.50 W (**b**) and 0.80 W (**c**). The frequency of the RF drive is 52.05 MHz. The magnetic field is 74 mT. The solid lines are fitting results combining a Rabi oscillation and exponential decays. For strong RF driving (**c**), the Rabi oscillation contains more than one frequency component and the faster oscillation term dominates. **d**, Rabi frequency as a function of RF driving power. The error bars show the standard deviations of data points. The microwave power is P_{MW} = 0.35 W. The external magnetic field is 74 mT.

triangular lattice of hBN are suitable for the large-scale quantum simulation of different magnetic states[15], including spin liquids[11,12]. Their coherence time can be improved further by reducing the temperature[45] and engineering strain and isotope compositions[48,49].

Online content

Any methods, additional references, Nature Research reporting summaries, source data, extended data, supplementary information, acknowledgements, peer review information; details of author contributions and competing interests; and statements of data and code availability are available at https://doi.org/10.1038/s41563-022-01329-8.

Received: 11 March 2022; Accepted: 7 July 2022;
Published online: 15 August 2022

References

1. Novoselov, K. S. et al. Electric field effect in atomically thin carbon films. *Science* **306**, 666–669 (2004).
2. Zhang, Y., Tan, Y.-W., Stormer, H. L. & Kim, P. Experimental observation of the quantum Hall effect and Berry's phase in graphene. *Nature* **438**, 201–204 (2005).
3. Cao, Y. et al. Unconventional superconductivity in magic-angle graphene superlattices. *Nature* **556**, 43–50 (2018).
4. Geim, A. K. & Grigorieva, I. V. Van der Waals heterostructures. *Nature* **499**, 419–425 (2013).
5. Novoselov, K., Mishchenko, A., Carvalho, A. & Castro Neto, A. 2D materials and van der Waals heterostructures. *Science* **353**, aac9439 (2016).
6. Kane, C. L. & Mele, E. J. Z_2 topological order and the quantum spin Hall effect. *Phys. Rev. Lett.* **95**, 146802 (2005).
7. Kane, C. L. & Mele, E. J. Quantum spin Hall effect in graphene. *Phys. Rev. Lett.* **95**, 226801 (2005).
8. Hasan, M. Z. & Kane, C. L. Colloquium: topological insulators. *Rev. Mod. Phys.* **82**, 3045–3067 (2010).
9. Gong, C. et al. Discovery of intrinsic ferromagnetism in two-dimensional van der Waals crystals. *Nature* **546**, 265–269 (2017).
10. Huang, B. et al. Layer-dependent ferromagnetism in a van der Waals crystal down to the monolayer limit. *Nature* **546**, 270–273 (2017).
11. Banerjee, A. et al. Proximate Kitaev quantum spin liquid behaviour in a honeycomb magnet. *Nat. Mater.* **15**, 733–740 (2016).
12. Chen, Y. et al. Strong correlations and orbital texture in single-layer 1T-$TaSe_2$. *Nat. Phys.* **16**, 218–224 (2020).
13. Liu, X. & Hersam, M. C. 2D materials for quantum information science. *Nat. Rev. Mater.* **4**, 669–684 (2019).
14. Kane, B. E. A silicon-based nuclear spin quantum computer. *Nature* **393**, 133–137 (1998).
15. Cai, J., Retzker, A., Jelezko, F. & Plenio, M. B. A large-scale quantum simulator on a diamond surface at room temperature. *Nat. Phys.* **9**, 168–173 (2013).
16. Gershenfeld, N. A. & Chuang, I. L. Bulk spin-resonance quantum computation. *Science* **275**, 350–356 (1997).
17. Lovchinsky, I. et al. Magnetic resonance spectroscopy of an atomically thin material using a single-spin qubit. *Science* **355**, 503–507 (2017).
18. Gottscholl, A. et al. Initialization and read-out of intrinsic spin defects in a van der Waals crystal at room temperature. *Nat. Mater.* **19**, 540–545 (2020).
19. Gottscholl, A. et al. Room temperature coherent control of spin defects in hexagonal boron nitride. *Sci. Adv.* **7**, eabf3630 (2021).
20. Abdi, M., Chou, J.-P., Gali, A. & Plenio, M. B. Color centers in hexagonal boron nitride monolayers: a group theory and ab initio analysis. *ACS Photonics* **5**, 1967–1976 (2018).
21. Ivády, V. et al. Ab initio theory of the negatively charged boron vacancy qubit in hexagonal boron nitride. *npj Comput. Mater.* **6**, 41 (2020).
22. Reimers, J. R. et al. Photoluminescence, photophysics, and photochemistry of the V_B^- defect in hexagonal boron nitride. *Phys. Rev. B* **102**, 144105 (2020).
23. Chejanovsky, N. et al. Single-spin resonance in a van der Waals embedded paramagnetic defect. *Nat. Mater.* **20**, 1079–1084 (2021).
24. Stern, H. L. et al. Room-temperature optically detected magnetic resonance of single defects in hexagonal boron nitride. *Nat. Commun.* **13**, 618 (2022).
25. Pakdel, A., Bando, Y. & Golberg, D. Nano boron nitride flatland. *Chem. Soc. Rev.* **43**, 934–959 (2014).
26. Kianinia, M., White, S., Froch, J. E., Bradac, C. & Aharonovich, I. Generation of spin defects in hexagonal boron nitride. *ACS Photonics* **7**, 2147–2152 (2020).
27. Gao, X. et al. High-contrast plasmonic-enhanced shallow spin defects in hexagonal boron nitride for quantum sensing. *Nano Lett.* **21**, 7708–7714 (2021).
28. Guo, N.-J. et al. Generation of spin defects by ion implantation in hexagonal boron nitride. *ACS Omega* **7**, 1733–1739 (2022).
29. Gao, X. et al. Femtosecond laser writing of spin defects in hexagonal boron nitride. *ACS Photonics* **8**, 994–1000 (2021).
30. Gottscholl, A. et al. Spin defects in hBN as promising temperature, pressure and magnetic field quantum sensors. *Nat. Commun.* **12**, 4480 (2021).
31. Healey, A. et al. Quantum microscopy with van der Waals heterostructures. Preprint at https://arxiv.org/abs/2112.03488 (2021).
32. Huang, M. et al. Wide field imaging of van der Waals ferromagnet Fe_3GeTe_2 by spin defects in hexagonal boron nitride. Preprint at https://arxiv.org/abs/2112.13570 (2021).
33. Dutt, M. G. et al. Quantum register based on individual electronic and nuclear spin qubits in diamond. *Science* **316**, 1312–1316 (2007).
34. Gangloff, D. et al. Quantum interface of an electron and a nuclear ensemble. *Science* **364**, 62–66 (2019).
35. Ruskuc, A., Wu, C.-J., Rochman, J., Choi, J. & Faraon, A. Nuclear spin-wave quantum register for a solid-state qubit. *Nature* **602**, 408–413 (2022).
36. Bermudez, A., Jelezko, F., Plenio, M. B. & Retzker, A. Electron-mediated nuclear-spin interactions between distant nitrogen-vacancy centers. *Phys. Rev. Lett.* **107**, 150503 (2011).
37. Ping, Y. & Smart, T. J. Computational design of quantum defects in two-dimensional materials. *Nat. Comput. Sci.* **1**, 646–654 (2021).
38. Smart, T. J., Li, K., Xu, J. & Ping, Y. Intersystem crossing and exciton–defect coupling of spin defects in hexagonal boron nitride. *npj Comput. Mater.* **7**, 59 (2021).
39. Wu, F., Galatas, A., Sundararaman, R., Rocca, D. & Ping, Y. First-principles engineering of charged defects for two-dimensional quantum technologies. *Phys. Rev. Mater.* **1**, 071001 (2017).
40. Mathur, N. et al. Excited-state spin-resonance spectroscopy of V_B^- defect centers in hexagonal boron nitride. *Nat. Commun.* **13**, 3233 (2022).
41. Baber, S. et al. Excited state spectroscopy of boron vacancy defects in hexagonal boron nitride using time-resolved optically detected magnetic resonance. *Nano Lett.* **22**, 461 (2022).
42. Yu, P. et al. Excited-state spectroscopy of spin defects in hexagonal boron nitride. *Nano Lett.* **22**, 3545–3549 (2022).
43. Mu, Z. et al. Excited-state optically detected magnetic resonance of spin defects in hexagonal boron nitride. *Phys. Rev. Lett.* **128**, 216402 (2022).
44. Jacques, V. et al. Dynamic polarization of single nuclear spins by optical pumping of nitrogen-vacancy color centers in diamond at room temperature. *Phys. Rev. Lett.* **102**, 057403 (2009).
45. Murzakhanov, F. F. Electron–nuclear coherent coupling and nuclear spin readout through optically polarized V_B^- spin states in hBN. *Nano Lett.* **22**, 2718–2724 (2022).
46. Chen, M., Hirose, M. & Cappellaro, P. et al. Measurement of transverse hyperfine interaction by forbidden transitions. *Phys. Rev. B* **92**, 020101 (2015).
47. Sangtawesin, S. et al. Hyperfine-enhanced gyromagnetic ratio of a nuclear spin in diamond. *New J. Phys.* **18**, 083016 (2016).
48. Lee, J., Park, H. & Seo, H. First-principles theory of extending the spin qubit coherence time in hexagonal boron nitride. Preprint at https://arxiv.org/abs/2202.04346 (2022).
49. Haykal, A. et al. Decoherence of V_B^- spin defects in monoisotopic hexagonal boron nitride. *Nat. Commun.* **13**, 4347 (2022).

Publisher's note Springer Nature remains neutral with regard to jurisdictional claims in published maps and institutional affiliations.

Methods

Sample preparation. Here hBN nanosheets were exfoliated from a high-quality hBN single crystal synthesized by a high-pressure process to 10–100 nm thickness with tapes and transferred onto a Si substrate. The sample was ion implanted using 2.5 keV helium ions with a dose of $10^{14}\,cm^{-2}$. Then, the hBN flakes with spin-active defects were transferred onto the silver co-planar waveguide (CPW) using a stamp consisting of a thin polycarbonate (PC) film mounted on a polydimethylsiloxane block on a glass slide. The hBN flakes and PC stamp were aligned and made to have contact using a micropositioner under a microscope. The temperature was raised up to 80 °C to make hBN flakes adhere to the PC film as it is lifted off the substrate. Then, a silver CPW was placed on the heater and aligned with the hBN flakes. After making the PC stamp and CPW come into contact, the temperature was slowly heated up to 150 °C, which allows the PC stamp to melt and attach onto the CPW. Finally, we lifted off the glass slide with the polydimethylsiloxane block and chloroform was used to dissolve the PC from the CPW. All the data shown in the main text were obtained from the same hBN nanosheet.

Experimental setup and ODMR measurement. All the measurements were carried out at room temperature using a home-built confocal microscope system. A 532 nm laser was sent through a 650 nm dichroic mirror and focused onto the sample using a high numerical aperture (NA = 0.9) objective lens with ×100 magnification. An acousto-optic modulator (ISOMET, M1205-T110L-1) was used as a fast optical switch. The photoluminescence was separated from the laser by a dichroic mirror and the residual laser light was blocked by two 550 nm long-pass filters. Afterwards, the photoluminescence was coupled into a single-mode optical fibre and guided to a single-photon counter (Excelitas, SPCM-AQRH). MWs are generated by a Stanford Research Systems SG386 signal generator. The amplitude is modulated by two fast RF switches (Mini-Circuits, ZASWA-2-50DRA+) and then amplified by amplifiers (Mini-Circuits, ZHL-10W-202s, ZHL-16W-43-S+ and ZVE-6W-83+). As the amplification factor depends on the frequency, we adjust the input MW power to compensate for this. The MW power measured at the output port of the CPW is calibrated a few times to minimize the frequency dependence of power fluctuation. For ODMR measurements, a pulse steamer (Swabian Instruments, Pulse Streamer 8/2) sends pulses to modulate the RF switches, signal generator and acousto-optic modulator. A permanent magnet was mounted on a linear translation stage behind the sample to apply a tunable external d.c. magnetic field perpendicular to the hBN flake surface. In ODNMR measurements, another Stanford Research Systems SG386 signal generator is used to generate the RF signal. Similarly, the amplitude is modulated by two fast RF switches (Mini-Circuits, ZASWA-2-50DRA+) and then amplified by an amplifier (Mini-Circuits, LZY-22+). Then, the RF signal is combined with the MW using a power splitter (Mini-Circuits, ZFRSC-42-S+).

Nuclear-spin polarization fitting. A seven Lorentzian fitting of the ODMR spectrum gives the population of each nuclear spin state. At low laser power, seven peaks are clearly resolved, which provide the frequency information of each hyperfine peak. Under high-power laser excitation, linewidth broadening makes it hard to resolve each peak. Therefore, we use the known frequencies obtained from the low-laser-power ODMR to fit the spectrum and determine the relative population of each nuclear spin state. Finally, the polarization is calculated using the fitted relative populations of the hyperfine basis states:

$$P_{\mathrm{exp}} = \frac{\sum_{m_I} m_I \rho_{m_I}}{3\sum_{m_I} \rho_{m_I}},$$

where the summation is performed over all the hyperfine peaks in the ODMR spectrum.

Ab initio calculation. In this work, we used the open-source plane-wave code Quantum Espresso (QE)[50] and the Vienna ab initio simulation package[51] to calculate the hyperfine parameters and compare the results. In the calculations by the Vienna ab initio simulation package, we used projector-augmented-wave pseudopotentials with a kinetic-energy cutoff of 500 eV for the wavefunctions. Atomic forces were converged to 0.001 eV Å^{-1} in geometry optimization. In the calculations by QE, we used the projector-augmented-wave pseudopotentials with a kinetic-energy cutoff of 55 Ry for the wavefunctions, which is sufficient to converge the hyperfine tensor (A). The default force threshold of 0.001 Ry Bohr^{-1} was set for geometry optimization. Three supercell sizes, namely, $6\times6\times1$, $8\times8\times1$ and $10\times10\times1$, were chosen to ensure the supercell size convergence of defect calculations. A single k-point (Γ) was sampled in the Brillouin zone for the supercell calculations. All the calculations were done with the Perdew–Burke–Ernzerhof exchange–correlation functional. The excited state was calculated with constrained-occupation density functional theory calculations. Spin density was obtained from the spin-up and spin-down difference of the defect-wavefunction module square. Finally, hyperfine parameters by QE were calculated by using the QE-GIPAW code.

Reporting summary. Further information on research design is available in the Nature Research Reporting Summary linked to this article.

Data availability

Source data are provided with this paper. All other data that support the plots within this paper and other findings of this study are available from the corresponding author upon reasonable request.

Code availability

The custom codes that support the findings of this study are available from the corresponding author upon reasonable request.

References

50. Giannozzi, P. et al. QUANTUM ESPRESSO: a modular and open-source software project for quantum simulations of materials. *J. Phys.: Condens. Matter* **21**, 395502 (2009).
51. Kresse, G. & Furthmüller, J. Efficient iterative schemes for ab initio total-energy calculations using a plane-wave basis set. *Phys. Rev. B* **54**, 11169 (1996).

Acknowledgements

T.L. thanks the Purdue Quantum Science and Engineering Institute (PQSEI) for support through the seed grant, the DARPA NLM program, the DARPA QUEST program and the National Science Foundation under grant no. PHY-2110591. Y.P. is supported by the National Science Foundation under grant no. DMR-1760260. A.E.L.A and Y.P.C. acknowledge support by the Quantum Science Center, a US Department of Energy, Office of Science, National Quantum Information Science Research Center. Y.P.C. also thanks the hospitality of NIMS and support of Tohoku AIMR and FriDUO program. B.J. and S.A.B. are supported by the Office of Naval Research (ONR) grant award no. N00014-20-1-2806. K.W. and T.T. acknowledge support from JSPS KAKENHI (grant nos. 19H05790, 20H00354 and 21H05233). The ab initio calculations used resources of the lux supercomputer at the University of California, Santa Cruz, funded by the National Science Foundation MRI grant no. AST 1828315; the Center for Functional Nanomaterials, which is a US Department of Energy, Office of Science, facility; and the Scientific Data and Computing center, a component of the Computational Science Initiative, at Brookhaven National Laboratory under contract no. DE-SC0012704.

Author contributions

T.L. and X.G. conceived and designed the project. X.G., Z.X., S.V., P.J. and K.S. built the setup. K.L., X.G. and S.V. performed the calculations. B.J. fabricated the MW waveguides. T.T. and K.W. grew the hBN crystals. X.G., S.V. and A.E.L.A. created the hBN nanosheets with spin defects. X.G. performed the measurements. X.G., T.L., S.V., K.L. and Y.P. analysed the results. T.L., Y.P., Y.P.C. and S.A.B supervised the project. All the authors contributed to the writing of the manuscript.

Competing interests

The authors declare no competing interests.

Additional information

Supplementary information The online version contains supplementary material available at https://doi.org/10.1038/s41563-022-01329-8.

Correspondence and requests for materials should be addressed to Tongcang Li.

Peer review information *Nature Materials* thanks Weibo Gao, Fedor Jelezko and the other, anonymous, reviewer(s) for their contribution to the peer review of this work.

Reprints and permissions information is available at www.nature.com/reprints.

nature portfolio

Corresponding author(s): Tongcang Li

Last updated by author(s): Jul 7, 2022

Reporting Summary

Nature Portfolio wishes to improve the reproducibility of the work that we publish. This form provides structure for consistency and transparency in reporting. For further information on Nature Portfolio policies, see our Editorial Policies and the Editorial Policy Checklist.

Statistics

For all statistical analyses, confirm that the following items are present in the figure legend, table legend, main text, or Methods section.

n/a	Confirmed	
☐	☒	The exact sample size (n) for each experimental group/condition, given as a discrete number and unit of measurement
☐	☒	A statement on whether measurements were taken from distinct samples or whether the same sample was measured repeatedly
☒	☐	The statistical test(s) used AND whether they are one- or two-sided *Only common tests should be described solely by name; describe more complex techniques in the Methods section.*
☒	☐	A description of all covariates tested
☒	☐	A description of any assumptions or corrections, such as tests of normality and adjustment for multiple comparisons
☒	☐	A full description of the statistical parameters including central tendency (e.g. means) or other basic estimates (e.g. regression coefficient) AND variation (e.g. standard deviation) or associated estimates of uncertainty (e.g. confidence intervals)
☒	☐	For null hypothesis testing, the test statistic (e.g. F, t, r) with confidence intervals, effect sizes, degrees of freedom and P value noted *Give P values as exact values whenever suitable.*
☒	☐	For Bayesian analysis, information on the choice of priors and Markov chain Monte Carlo settings
☒	☐	For hierarchical and complex designs, identification of the appropriate level for tests and full reporting of outcomes
☒	☐	Estimates of effect sizes (e.g. Cohen's d, Pearson's r), indicating how they were calculated

Our web collection on statistics for biologists contains articles on many of the points above.

Software and code

Policy information about availability of computer code

Data collection	Data collection was done with customized programs written in LabVIEW.
Data analysis	All fits to the data were made with the commercial software Matlab. The fit functions and Matlab codes used for simulation can be made available upon request. The first-principles calculations for obtaining hyperfine parameters were carried out using the open source plane-wave code Quantum Espresso (QE) and the Vienna Ab-initio Simulation package (VASP). The excited state was calculated with constrained-occupation density-functional theory.

For manuscripts utilizing custom algorithms or software that are central to the research but not yet described in published literature, software must be made available to editors and reviewers. We strongly encourage code deposition in a community repository (e.g. GitHub). See the Nature Portfolio guidelines for submitting code & software for further information.

Data

Policy information about availability of data

All manuscripts must include a data availability statement. This statement should provide the following information, where applicable:

- Accession codes, unique identifiers, or web links for publicly available datasets
- A description of any restrictions on data availability
- For clinical datasets or third party data, please ensure that the statement adheres to our policy

Source data are provided with this paper. All other data that support the plots within this paper and other findings of this study are available from the corresponding authors upon reasonable request.

March 2021

Field-specific reporting

Please select the one below that is the best fit for your research. If you are not sure, read the appropriate sections before making your selection.

☐ Life sciences ☐ Behavioural & social sciences ☐ Ecological, evolutionary & environmental sciences

For a reference copy of the document with all sections, see nature.com/documents/nr-reporting-summary-flat.pdf

Life sciences study design

All studies must disclose on these points even when the disclosure is negative.

Sample size	*Describe how sample size was determined, detailing any statistical methods used to predetermine sample size OR if no sample-size calculation was performed, describe how sample sizes were chosen and provide a rationale for why these sample sizes are sufficient.*
Data exclusions	*Describe any data exclusions. If no data were excluded from the analyses, state so OR if data were excluded, describe the exclusions and the rationale behind them, indicating whether exclusion criteria were pre-established.*
Replication	*Describe the measures taken to verify the reproducibility of the experimental findings. If all attempts at replication were successful, confirm this OR if there are any findings that were not replicated or cannot be reproduced, note this and describe why.*
Randomization	*Describe how samples/organisms/participants were allocated into experimental groups. If allocation was not random, describe how covariates were controlled OR if this is not relevant to your study, explain why.*
Blinding	*Describe whether the investigators were blinded to group allocation during data collection and/or analysis. If blinding was not possible, describe why OR explain why blinding was not relevant to your study.*

Behavioural & social sciences study design

All studies must disclose on these points even when the disclosure is negative.

Study description	*Briefly describe the study type including whether data are quantitative, qualitative, or mixed-methods (e.g. qualitative cross-sectional, quantitative experimental, mixed-methods case study).*
Research sample	*State the research sample (e.g. Harvard university undergraduates, villagers in rural India) and provide relevant demographic information (e.g. age, sex) and indicate whether the sample is representative. Provide a rationale for the study sample chosen. For studies involving existing datasets, please describe the dataset and source.*
Sampling strategy	*Describe the sampling procedure (e.g. random, snowball, stratified, convenience). Describe the statistical methods that were used to predetermine sample size OR if no sample-size calculation was performed, describe how sample sizes were chosen and provide a rationale for why these sample sizes are sufficient. For qualitative data, please indicate whether data saturation was considered, and what criteria were used to decide that no further sampling was needed.*
Data collection	*Provide details about the data collection procedure, including the instruments or devices used to record the data (e.g. pen and paper, computer, eye tracker, video or audio equipment) whether anyone was present besides the participant(s) and the researcher, and whether the researcher was blind to experimental condition and/or the study hypothesis during data collection.*
Timing	*Indicate the start and stop dates of data collection. If there is a gap between collection periods, state the dates for each sample cohort.*
Data exclusions	*If no data were excluded from the analyses, state so OR if data were excluded, provide the exact number of exclusions and the rationale behind them, indicating whether exclusion criteria were pre-established.*
Non-participation	*State how many participants dropped out/declined participation and the reason(s) given OR provide response rate OR state that no participants dropped out/declined participation.*
Randomization	*If participants were not allocated into experimental groups, state so OR describe how participants were allocated to groups, and if allocation was not random, describe how covariates were controlled.*

Ecological, evolutionary & environmental sciences study design

All studies must disclose on these points even when the disclosure is negative.

Study description	*Briefly describe the study. For quantitative data include treatment factors and interactions, design structure (e.g. factorial, nested, hierarchical), nature and number of experimental units and replicates.*
Research sample	*Describe the research sample (e.g. a group of tagged Passer domesticus, all Stenocereus thurberi within Organ Pipe Cactus National*

Research sample	*Monument), and provide a rationale for the sample choice. When relevant, describe the organism taxa, source, sex, age range and any manipulations. State what population the sample is meant to represent when applicable. For studies involving existing datasets, describe the data and its source.*
Sampling strategy	*Note the sampling procedure. Describe the statistical methods that were used to predetermine sample size OR if no sample-size calculation was performed, describe how sample sizes were chosen and provide a rationale for why these sample sizes are sufficient.*
Data collection	*Describe the data collection procedure, including who recorded the data and how.*
Timing and spatial scale	*Indicate the start and stop dates of data collection, noting the frequency and periodicity of sampling and providing a rationale for these choices. If there is a gap between collection periods, state the dates for each sample cohort. Specify the spatial scale from which the data are taken*
Data exclusions	*If no data were excluded from the analyses, state so OR if data were excluded, describe the exclusions and the rationale behind them, indicating whether exclusion criteria were pre-established.*
Reproducibility	*Describe the measures taken to verify the reproducibility of experimental findings. For each experiment, note whether any attempts to repeat the experiment failed OR state that all attempts to repeat the experiment were successful.*
Randomization	*Describe how samples/organisms/participants were allocated into groups. If allocation was not random, describe how covariates were controlled. If this is not relevant to your study, explain why.*
Blinding	*Describe the extent of blinding used during data acquisition and analysis. If blinding was not possible, describe why OR explain why blinding was not relevant to your study.*

Did the study involve field work? ☐ Yes ☒ No

Reporting for specific materials, systems and methods

We require information from authors about some types of materials, experimental systems and methods used in many studies. Here, indicate whether each material, system or method listed is relevant to your study. If you are not sure if a list item applies to your research, read the appropriate section before selecting a response.

Materials & experimental systems

n/a	Involved in the study	
☒	☐	Antibodies
☒	☐	Eukaryotic cell lines
☒	☐	Palaeontology and archaeology
☒	☐	Animals and other organisms
☒	☐	Human research participants
☒	☐	Clinical data
☒	☐	Dual use research of concern

Methods

n/a	Involved in the study	
☒	☐	ChIP-seq
☒	☐	Flow cytometry
☒	☐	MRI-based neuroimaging